

Self-Contained Monolithic Carbon Sponges for Solar-Driven Interfacial Water Evaporation Distillation and Electricity Generation

Liangliang Zhu, Minmin Gao, Connor Kang Nuo Peh, Xiaoqiao Wang, and Ghim Wei Ho*

Solar vaporization has received tremendous attention for its potential in desalination, sterilization, distillation, etc. However, a few major roadblocks toward practical application are the high cost, process intensive, fragility of solar absorber materials, and low efficiency. Herein an inexpensive cellular carbon sponge that has a broadband light absorption and inbuilt structural features to perform solitary heat localization for in situ photothermic vaporization is reported. The defining advantages of elastic cellular porous sponge are that it self-confines water to the perpetually hot spots and accommodates cyclical dynamic fluid flow-volume variable stress for practical usage. By isolating from bulk water, the solar-to-vapor conversion efficiency is increased by 2.5-fold, surpassing that of conventional bulk heating. Notably, complementary solar steam generation-induced electricity can be harvested during the solar vaporization so as to capitalize on waste heat. Such solar distillation and waste heat-to-electricity generation functions may provide potential opportunities for on-site electricity and fresh water production for remote areas/emergency needs.

Solar-driven vaporization is emerging as one of the most promising solar thermal technologies for its potential applications in domestic water heating, purification, distillation, seawater desalination, and electricity generation.^[1–6] Though significant progress has been made to enhance solar mediated water evaporation based on heat harvesting by solar thermal absorber materials, many challenges remain to be overcome. Seemingly,

most of the designed solar thermal absorbers involve either costly materials such as plasmonic noble metal nanostructures or extensive fabrication processes—critical-point or freeze drying, with a poor perspective of manufacturing cost and scalability.^[7–14] Moreover, the light-to-heat conversion is commonly demonstrated with membranes, paper, thin film-based material systems, which need to be in continual and direct contact with the bulk water.^[15–19] Hence, immense heat losses persist in the nonevaporative part of the bulk fluid driven by thermal diffusion.^[10,20] Meanwhile, carbon-based solar absorber materials are gaining attention in view of its intrinsic broadband light absorption, excellent photothermal conduction, and low thermal emission, which is promising for efficient solar-driven vaporization.^[15,21,22] Furthermore, carbon materials display good photostability in a

wide wavelength range, biodegradability, and low toxicity attributes that are essential for future technological translation.^[23–26] Different forms of carbon, i.e., carbon nanotubes, graphene-based aerogel, exfoliated graphite layer, etc., have been successfully developed as solar absorber materials.^[19,27,28] However, the carbon nanostructures are often susceptible to aggregation in aqueous solution and are structurally fragile due to dynamic fluid flow and volume variations stress. This has restricted the materials lifetime associated to mechanical deterioration for repetitive usage. Till date, there is no report on the design of low-cost, mechanically robust, and self-contained, a truly heat localized solar-vaporization sponge that can operate efficiently in isolation, completely cut off from the bulk water supply.

Herein, we make use of an ultralight weight nitrogen-enriched carbon sponge (CS), a 3D elastic cellular solid to soak up water and perform efficient in situ photothermic vaporization. The CSs possess a favorable inbuilt structural hierarchy with mesoporous fibers that are seamlessly interconnected to form elastic macroporous open cells. We exploit the sponge capillary action to wick and confine the liquid within the vicinity of perpetually hot spots so as to deliberately isolate from the bulk water body. By doing so, the bulk water heat losses are eliminated and markedly enhanced in situ photothermic vaporization can be realized. Notably, the hierarchical cellular

Dr. L. L. Zhu, Dr. M. M. Gao, Dr. C. K. N. Peh, Dr. X. Q. Wang,
Prof. G. W. Ho

Department of Electrical and Computer Engineering
National University of Singapore
4 Engineering Drive 3, 117583, Singapore
E-mail: elehgw@nus.edu.sg

Prof. G. W. Ho
Engineering Science Programme
National University of Singapore
9 Engineering Drive 1, 117575, Singapore

Prof. G. W. Ho
Institute of Materials Research and Engineering
A*STAR (Agency for Science, Technology and Research)
3 Research Link, 117602, Singapore

 The ORCID identification number(s) for the author(s) of this article can be found under <https://doi.org/10.1002/aenm.201702149>.

DOI: 10.1002/aenm.201702149

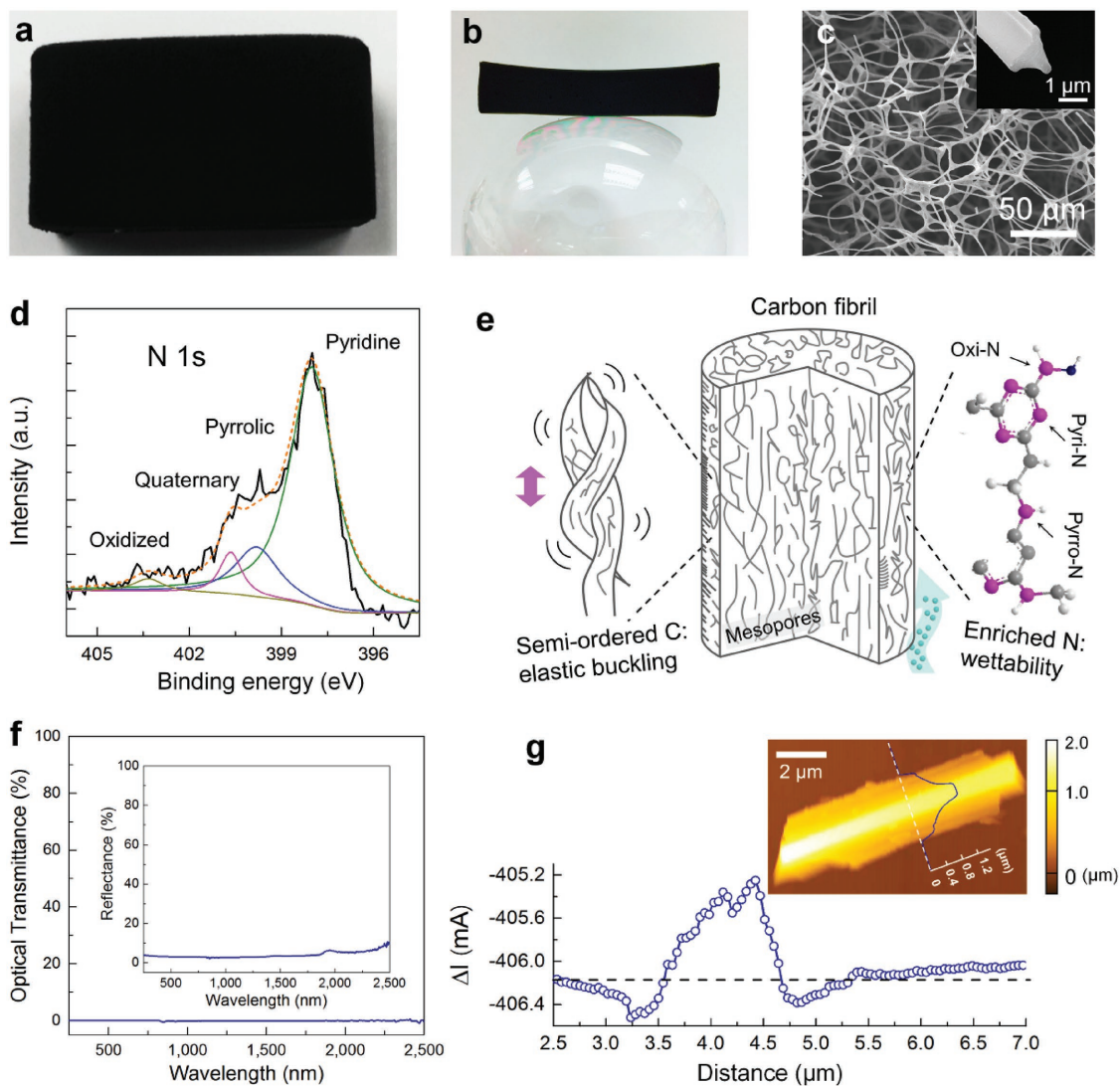


Figure 1. Morphologies and characterizations of CS. a) Photograph of a piece of CS. b) Photograph of a CS block standing on the bubble balloon. c) SEM images of CS, inset: corresponding cross-sectional image of CS fibrils. d) High-resolution XPS spectra of CS for N 1s. e) Schematic diagrams of the CS fibril. f) Transmittance and reflectance spectra of CS. g) AFM image of the CS fibril on a silicon substrate and the probe current signal profile along the blue line of the CS fibril SThM image in Figure S14b in the Supporting Information.

pore structure of the CS is essential in maintaining its viability in water wicking-holding and consequently its elasticity capabilities to adapt the mechanical water absorption–expansion and evaporation–contraction stress. Subsequently, we present the first ever demonstration of the self-contained CS for solar-driven interfacial water evaporation distillation and complementary waste heat-to-energy generation. Prototypes of small-form outdoor photothermic solar distillation systems based on our CS are also shown both on land and water bodies. This work provides a new opportunity for generating fresh water, and electricity, on-site/on-demand which is especially attractive for remote rural areas.

Scalable CS is easily prepared by a straightforward thermal carbonization of a low-cost melamine polymer precursor. CS presents an ideal nonaggregated porous structure of carbon fibrils network with open-cell pores for nonrestrictive mass

transfer. The as-prepared monolithic block of cellular sponge possesses in-built elastic, ultralightweight and structural hierarchy with mesoporous fibers that are seamlessly interconnected to form a macroporous open cell (**Figure 1a–c**). Scanning electron microscopy (SEM) images in **Figure 1c** reveal that the CS inherits reticulated cellular network with tunable open-cell pores dimension and diameter of the fibrils. The average pore sizes of 55, 45, and 25 μm were achieved under carbonization temperatures of 500, 700, and 900 °C which is referred to as CS55, CS45, and CS25, respectively (**Figures S1 and S2**, Supporting Information). The concave triangular cross-section fibrils were formed during the carbonization process. Noticeably, the diameter of the fibrils decreased from ≈2.1 μm (CS55), 1.6 μm (CS45) to 1.3 μm (CS25) (**Figure 1c** and **Figure S1**, Supporting Information, insets). N₂ adsorption–desorption measurements obtained from CS25 gave a specific surface area

of $551.1 \text{ m}^2 \text{ g}^{-1}$, pore size distribution of 1–4 nm, and total pore volume of $0.096 \text{ cm}^3 \text{ g}^{-1}$ (Figure S3, Supporting Information), suggesting mesoporous fibrils. The formation of mesopores is attributed to the nitrogen atoms released as N_2 and NH_3 gases during the carbonization process.^[29]

The chemical compositions of melamine polymer precursor and CSs were also confirmed by Fourier transform infrared (FTIR) spectrometry and energy dispersive X-ray. FTIR data suggest an enhancement in degree of carbonization in the CSs (Figure S4, Supporting Information). The elemental analysis results (Figure S5 and Table S1, Supporting Information) indicate that CSs are carbon and nitrogen-rich products. The chemical states of the CS25 are clearly distinguished based on X-ray photoelectron spectroscopy (XPS) analysis presented in Figure 1d and Figure S6 in the Supporting Information. In the N1s spectrum, it can be fitted into four peaks using the Gaussian method, which indicated four components attributed to pyridinic nitrogen (N-6), pyrrolic (N-5), quaternary (N-Q), and oxidized pyridinic nitrogen (N-X).^[30,31] The characteristic graphitic feature in the CSs is also confirmed by Raman data and X-ray diffraction spectra (Figures S7 and S8, Supporting Information, and the detailed analysis next to the figures). In addition, incomplete ring-layered nanostructured carbon is seen from transmission electron microscopy image (Figure S9, Supporting Information), which reveals distinctive presence of semi-ordered carbonaceous material. Based on the aforementioned findings, the CS is identified as a nitrogen-enriched carbonaceous material inherited from melamine polymer precursor, which enables vital functions of enhanced light harvesting and improved wettability.^[15,32] Besides, rich nitrogen atoms in the graphitic matrix may have led to the favorable formation of kinks (semi-ordered carbon segments) which could exhibit a certain degree of plastic deformation, bearing the elasticity nature of the CS (Figure 1e).^[33] The high elasticity attribute is critical in preventing water cavitation or collapse of the CS pores under pressure and allowing it to buffer shape changes under dynamic fluid flow.

The CS (with a thickness of 4 mm) exhibits extremely small optical transmittance ($\approx 0.1\%$) and reflectance ($\approx 3\text{--}5\%$) in the visible and near infrared regions, indicating the large optical extinction of the CS (Figure 1f).^[9,15] The large extinction owes to the optical absorption of the graphitic carbon and the light scattering from the nanoscale fibrils that increases the optical path length within the CS. The large optical extinction characteristic of the foam structure associated with the excellent photothermal activity of carbon makes CS a desirable candidate for solar steam generation. With such a high absorption capability, the CS has potential to produce high photothermal efficiency. Scanning thermal microscopy (SThM) based on atomic force microscopy (AFM) technique was employed to probe thermal properties at the nanoscale level.^[34–36] The concave triangular cross-section of the carbon fibril can be observed by AFM tapping-mode (Figure 1g and Figure S10, Supporting Information). In conductivity contrast microscopy mode, a CS45 fibril on the silicon substrate was imaged using the nanothermal probe. The apparent probe current signal (ΔI) of carbon fibril can be detected from the silicon substrate with a set probe voltage of 250 mV heating the probe tip (Figure 1g). Three other common carbon materials with different thermal

conductivity—carbon black, carbon nanotubes, and graphite were also scanned under the same conditions in order to estimate the thermal conductivity of CS (Figures S11–S13, Supporting Information). The corresponding relative probe current profiles across the conductivity maps (Figure S14, Supporting Information) indicate that the probe current signal of the CS45 fibril is similar to graphite, which is regarded as one of the high thermal conductive carbon materials.^[37] Hence, our CS samples are capable of speeding up heat conduction and transfer from CS to water essential for solar vaporization.

The outstanding light absorption of CS provides unique opportunities for developing highly efficient solar–thermal systems.^[16,38] As a proof of concept, we demonstrate solar-driven water evaporation using the CS. Under solar radiation, the CS can efficiently heat up the air/water interface region and generate steady stream of steam escaping from the CS surface (Figure S15 and Movie S1, Supporting Information). High-speed camera is also employed to enable real-time monitoring of the steam generation (Figure S16, Supporting Information). Zooming into the surface of the CS, mist or aerosol vapor droplets, often referred to wet steam are observed to be generated and escaped to the ambient continuously (Movie S2, Supporting Information). By collecting the condensed water, distillation and water purification are viable using sunlight as the sole energy source. Next, the open-cell structure with high wettability fibrils of the CS that forms interconnected pore channels is demonstrated to efficiently wick the bulk water to the surface of CS by capillary force (Figure 2a). The red-ink water is readily wicked and transported to the top of the CS. Evidently, a white piece of tissue paper placed on the CS turned red due to the soaking of the wicked red-ink water. Hence, the superior capillary action of the CS ensures continuous replenishment of water supply to the hot regions for enhanced photothermal vaporization. Moreover, the open cellular structure of CS is proven to be highly elastic with perfect shape recovery after compression (Figure 2b). The elasticity attribute is essential for sustenance of volume variation buffering during cyclical water absorption–expansion and evaporation–contraction process.

Due to its lightweight nature, the CS stays afloat at the water–air interface to enable interfacial water heating under light irradiation, evidently shown in the temperature–distance plot (Figure 2c,d and Figure S17, Supporting Information). Clearly, the CS displays localized sharp increase in temperature profile in contrast to a homogeneous water temperature profile that suggests bulk water heating in the absence of CS. Next, the evaporation rates of the CSs were quantified by measuring the weight loss of water with time (Figure 2e and Figure S18, Supporting Information). The rate of the evaporation for blank, CS55, CS45, and CS25 are 0.44, 1.12, 1.15, and $1.31 \text{ kg m}^{-2} \text{ h}^{-1}$ after 1 h evaporation stabilization. The respective conversion efficiencies (η) are calculated to be 25%, 72%, 74%, and 85% (Equations (S1) and (S2), Supporting Information). It is apparent that CS improves the solar–thermal conversion efficiency for steam generation. Amongst the various open-cell pore dimensions, the smallest pore size of $25 \mu\text{m}$ shows the highest water evaporation rate of $1.31 \text{ kg m}^{-2} \text{ h}^{-1}$. The attained evaporation rate is three times higher than that of bare water (blank) and 14–17% higher than that of CSs with larger pore size due to its denser fibrils network. Moreover, the surface

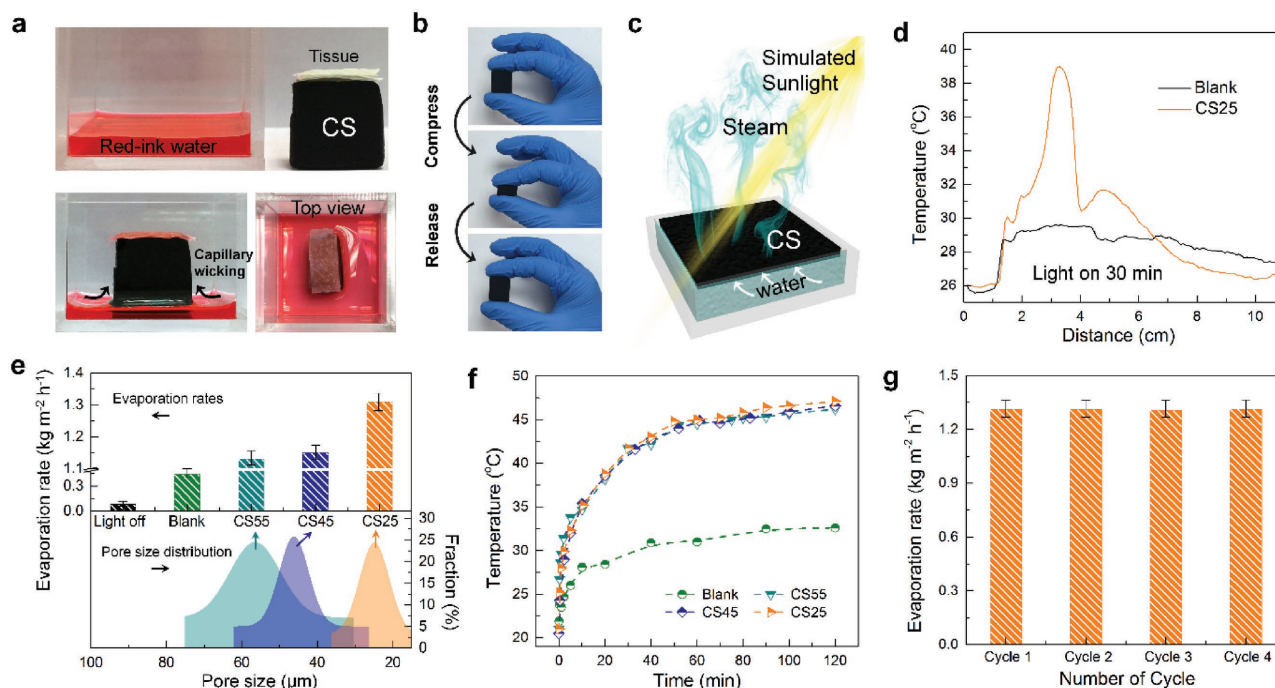


Figure 2. a) Photograph of red-ink water and several layers of tissue placed on the top of CS25 before wicking. Lower: The side and top views of the CS25 after wicking the red ink. b) Photographs of a block of CS25 compressed by fingertips. c) The schematic illustration of solar steam generation. d) Temperature profiles of water–air interface with and without CS25 under light irradiation for 30 min at an optical density of 1 kW m^{-2} . The evaporation rates e) and surface temperature changes f) of different CS over time at an optical density of 1 kW m^{-2} . g) Stability and reusability of CS25 for steam generation.

temperature of CS is $\approx 47 \text{ }^\circ\text{C}$ which is $\approx 14.4 \text{ }^\circ\text{C}$ higher than that of bulk water without CSs (Figure 2f). The results indicate heat localization or confinement at the evaporative CS surface minimized heat loss and augmented solar–thermal conversion efficiency. Furthermore, the CS is mechanically stable and robust for reusability and recycling without obvious degradation of water evaporation ability (Figure 2g). In a nutshell, the CS delivers broadband optical absorption and desirable in built structural features for solar heat localization, water transport–vapor escape accessibilities, and elastic matrix for durable solar-driven water evaporation performance.

To further explore the influence of localized heating on vaporization, we examined CS in four operation modes: contact (sinking, suspending, and floating) and completely isolated (containing) from the bulk water (Figure 3a–d and Figures S19 and S20, Supporting Information). In the context of CS in contact with the bulk water, the vaporization rates under 1 sun in the sinking, suspending, and floating configurations were determined to be 0.77 , 1.18 , and $1.39 \text{ kg m}^{-2} \text{ h}^{-1}$, respectively, which correspond to conversion efficiencies of 47%, 76%, and 90%, competitive with other carbon-based materials. (Figure 3e and Table S2, Supporting Information). Accordingly, their infrared images (Figure 3h–j) and respective temperature profiles (Figure 3f) were obtained. In the sinking configuration, the CS exhibits a uniform temperature distribution that implies bulk water heating scheme (Figure 3f, olive and Figure S21, Supporting Information). Due to the entire immersion of CS in water, the bulk water not only obstructs the light penetration and vapor exchange resulting in lower light absorbance and water

evaporation but also adversely transfers thermal heat to the bulk water leading to the excessive energy losses and decrease in vaporization efficiency. Comparatively, the considerably higher vaporization efficiencies of the suspending and floating CS indicate enhanced heat localization as opposed to the sinking CS. As such, heat is seen to concentrate on the surface of the suspending and floating CS at the air–water interface while the bulk water is conserved at a lower temperature (Figure 3f, orange and blue). It is noted that the temperature of the bulk water for the floating CS is lower than that of the suspending CS because of the reduction of contact area which diminishes the heat transfer between the CS and bulk water. Also, the highest temperature attained by the floating CS is observed to be lower than the suspending CS attributed to the higher surface evaporation. Considering both the lower bulk temperature and higher surface evaporation factors, the floating CS indeed displays the highest vaporization efficiency among the three configurations where CS are in contact with the bulk water.

Coming to the containing mode (i.e., completely isolated from the bulk water), we were motivated to further localize the heat. We exploit the CS to directly wick and confine water within its hierarchical cellular pore structure to perform in situ photothermic vaporization (Figure 3d and Figure S20, Supporting Information). In this way, the CS serves as a truly heat localized solar-vaporization sponge that operates in seclusion. Thus, the bulk water heat losses are largely phased out, leading to consequential photothermic vaporization. Notably, the surface temperature of CS (Figure 3f, purple) is the highest among all other configurations due to

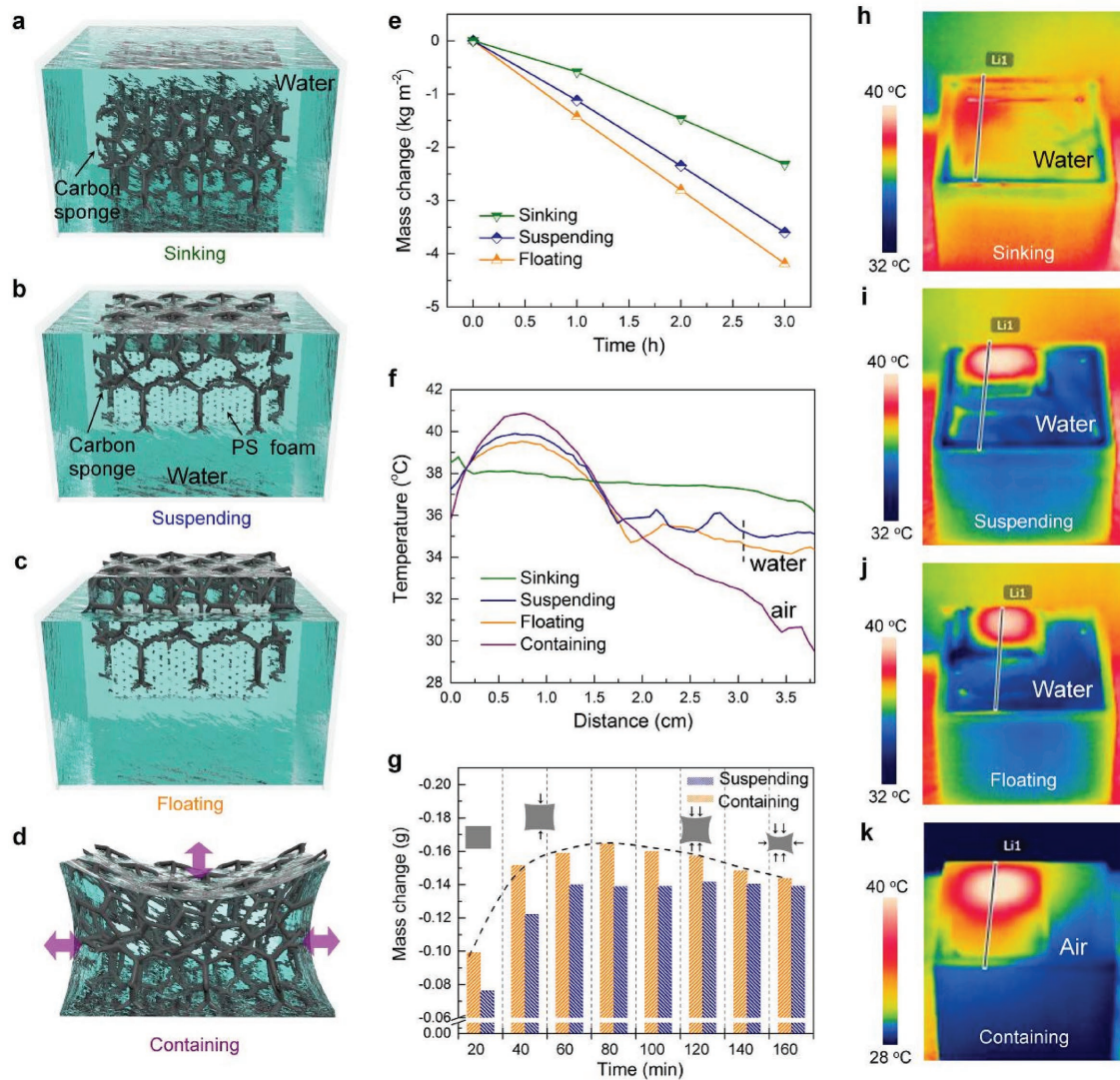


Figure 3. Schematic diagrams of CS in various configurations a) sinking, b) suspending, c) floating, and d) containing. e) The evaporation mass loss of sinking, suspending, and floating CS over time. f) Temperature profiles of the marked lines in infrared images (h–k) of different configurations after 30 min light irradiation. g) The evaporation mass loss comparison of CS in contact and completely isolated from bulk water. The insets show self-contained CS volume change with evaporation time.

the unsurpassed localized interfacial heating effect. This corroborates with the significant enhancement in vaporization rate of CS in the containing configuration as compared to that in the water (Figure 3g). The vaporization rate increases up to 118% in the first 80 min, after which the increment attenuate to 103.3% in the next 80 min owing to the excessive reduction of water contained in the CS. Importantly, the CS is able to regain its high vaporization rate of 118% upon water replenishment (Figure S22, Supporting Information). One other observation is that the CS shrinks along with the decreasing water content and conversely swells to recover to its original state after water replenishment. This is ascribed to its favorable elastic and hydrophilic fibrils network of cellular pore structure, which manifests as a mechanically outstanding and reusable sponge. All these findings unambiguously demonstrate the true localized interfacial heating of self-contained CS

which presents an energy- and cost-efficient strategy for solar-driven vaporization.

Given the steam generation capability of the CS, we are interested in scavenging the dynamic mechanical and temperature fluctuations for waste energy-to-electricity conversion. To do this, we used a ferroelectric fluoropolymer polyvinylidene fluoride (PVDF) to harvest the thermomechanical responses from the CS solar-vaporization (Figure 4a),^[39] which is the first demonstration of solar steam generation-induced electric potential. The coupling of the pyroelectric and piezoelectric effects is measured via heating–cooling and slight oscillation of PVDF film during the evaporation transition. The electrical signal outputs of CS undergoing water evaporation-induced piezo-pyroelectric responses and the temperature variations are recorded in Figure 4b–d. The maximum open circuit voltage (V_{oc}) and short circuit current (I_{sc})

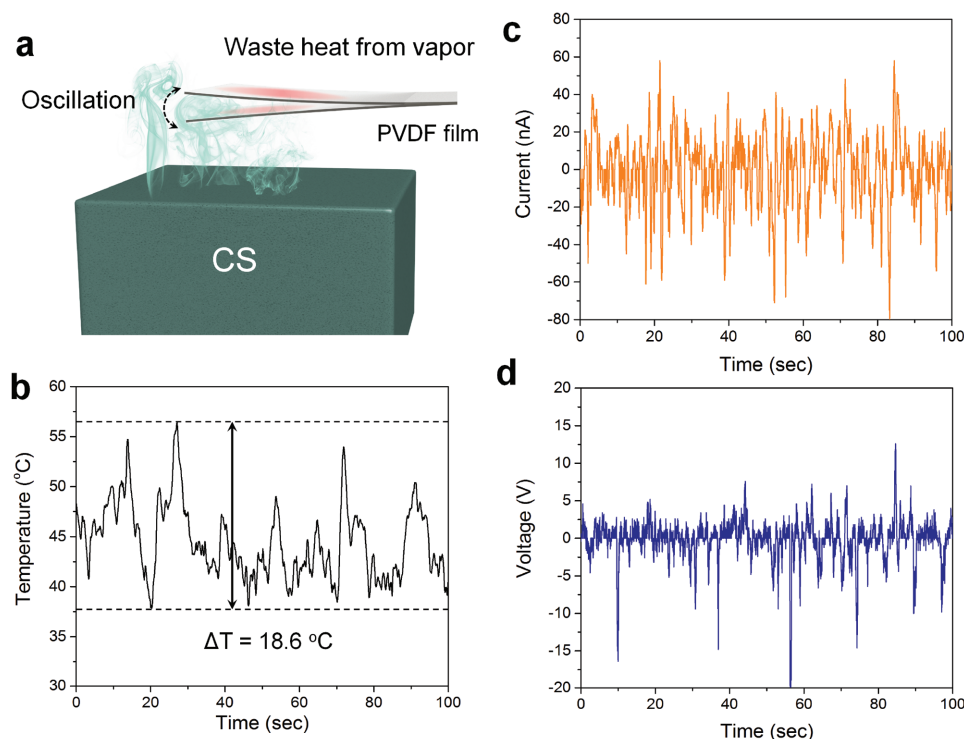


Figure 4. a) Schematic diagram of steam generation-induced electric potential by CS25. b) The temperature fluctuations of the PVDF film surface. The piezo-pyroelectric output currents c) and voltages d) of the PVDF films during the evaporation process.

obtained are -80 nA and -20 V, respectively (Figure 4c,d), which is resulted from the temperature fluctuation derived from heating-cooling variation of PVDF film (Figure 4b). The close matching of the measured electrical signal and the temperature change experienced by the PVDF film, as shown in Figure S23 in the Supporting Information, suggests that the pyroelectric effect is the predominant mechanism which is schematically presented in Figure S24 in the Supporting Information.^[39,40] The heating-cooling variation originates from the fluctuations of the generated steam caused by natural air flow, as shown in Movie S1 in the Supporting Information. Water vapor that reaches the surface of PVDF film, condenses to form numerous tiny water droplets and releases heat to the PVDF film. When the vapor drifts away, the local humidity around the PVDF film decreases and the tiny water droplets would quickly evaporate bringing about cooling to the PVDF film.^[39,41] The peak output voltage, current, and power were measured using an external loading resistance (Figure S25, Supporting Information). As the loading resistance increases, the output current decreases, while the output voltage increases (Figure S25a, Supporting Information). The calculated output power ascends and then descends with the increase of the loading resistance (Figure S25b, Supporting Information) and the highest output power of $240.7 \mu\text{W m}^{-2}$ was obtained. This approach provides an alternative strategy to harvest waste energy from solar vaporization for electricity generation, which effectively utilizes sustainable sunlight to trigger temporal motion and temperature dynamism.

To explore practical application of CS, outdoor water evaporation experiments were carried out to validate the solar steam

generation under natural sunlight conditions.^[17,42] A model house of dimensions $40 \text{ cm} \times 30 \text{ cm} \times 35 \text{ cm}$ was constructed using transparent acrylic to perform solar vaporization rate of self-contained CSs (Figure 5a). The infrared image of the Figure 5b shows heat localization of the CS which can effectively be employed as a photothermic sponge for solar steam distillation. Figure 5c shows the various measurements taken on a partly sunny day with roaming cloud (from 10:50 a.m. to 1:50 p.m., 19 April 2017), which caused the solar flux to vary dramatically ($\approx 150\text{--}1200 \text{ W m}^{-2}$). The outdoor time-dependent solar intensity was monitored while the corresponding CS surface and ambient temperatures as well as the evaporation mass changes were recorded (Figure 5c). Under the real sun and sky condition, it is apparent that a bare and completely exposed CS shows an efficient solar-thermal conversion which can easily reach to more than 78°C in 20 min (Figure S26, Supporting Information). And when the CS was soaked up with water and then placed inside the constructed solar still, the temperature can nonetheless reach up to 48.5°C (Figure 5c, blue). The surface temperature of the self-contained CS was observed to be consistently higher than the ambient air temperature after 5 min of sunlight irradiation (Figure 5c, olive). It can also be observed that the CS temperature varied with the solar intensity. During the extended period of intermittent cloud cover at 70–110 min period, the self-contained CS temperature dipped by 6.4°C , after which it picked up fairly rapid when the solar intensity is back to 1 sun owing to reasonably rapid interfacial heating characteristics of CS. This attribute is particularly useful for regions with ever changing solar insolation due to cloud cover etc. since it can benefit from fast localized interfacial heating

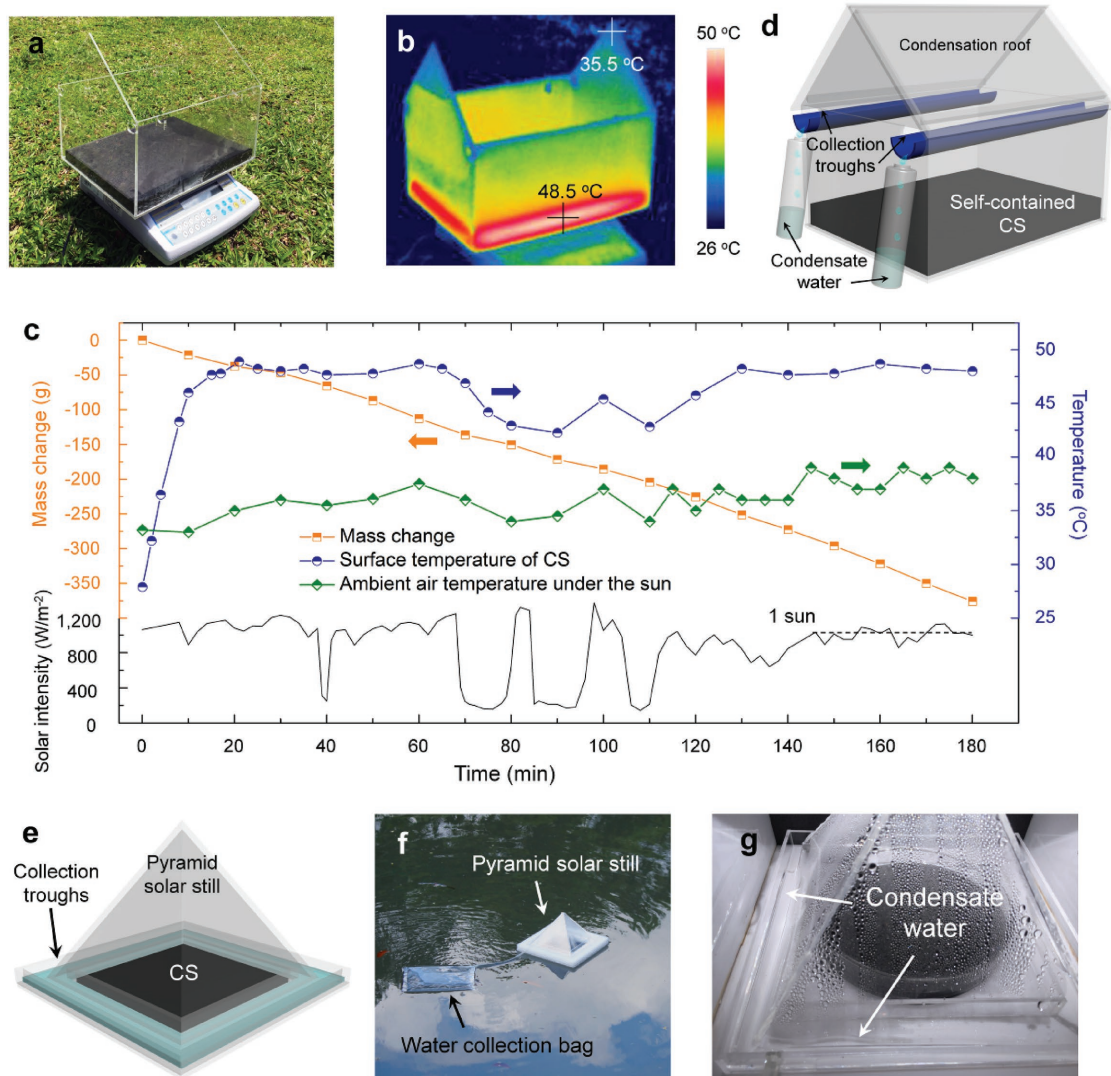


Figure 5. a) Photograph and b) infrared image of the solar still after 30 min sun irradiation. c) The solar intensity spectra, evaporation mass loss, and synchronous temperature changes of CS surface and ambient air under the sun from 10:50 a.m. to 1:50 p.m. on 19 April 2017 at National University of Singapore, Kent Ridge campus. d) Schematic diagrams of a model house solar still. Schematic diagrams e) and photograph of a pyramid solar still floating on water. g) The photograph of condensate water in the troughs of the pyramid solar still.

to expedite photothermic vaporization. Notably, the water mass change showed continuous decrease regardless of the cloud cover. The maximum water evaporation rate of $1.15 \text{ kg m}^{-2} \text{ h}^{-1}$ is achieved with an effective area of 0.0819 m^2 (Figure 5c, orange) which is of lower evaporation rate than that of the laboratory measurements. This is expected since the real outdoor conditions are subjected to varying incident solar flux which resulted in a decrease evaporation rate.^[1]

Furthermore, two potential simple and passive prototypes for solar distillation and condensate collection are presented herein. The model house with collection troughs and bottles as well as a pyramid solar still with side length of 16 cm with condensate collection troughs and bag was designed for land and water applications, respectively (Figure 5d–f and Figures S27 and S28, Supporting Information). Evidently, condensate water droplets can be observed in the collection troughs (Figure 5g). Consider the low-cost and portability, the passive solar stills

show practical feasibility of localized vaporization under ambient outdoor conditions, especially valuable for remote rural regions or areas experiencing emergency situations and natural disasters where drinking water supply is temporarily interrupted.

In summary, we have demonstrated high-efficiency in situ consequential photothermic vaporization by employing scalable 3D elastic cellular nitrogen-enriched CS. The CS has a broadband optical absorption and desirable inbuilt elastic cellular pore structure that maintains its viability in wicking-holding of water and accommodating cyclical dynamic fluid flow-volume variable stress. The self-contained CS serves as a truly heat localized solar-vaporization sponge that confines water to the perpetually hot spots. By doing so, excessive heat losses to nonevaporative bulk water that limit the efficiency of vaporization are eliminated. Notably, the self-contained CS also exhibits solar steam generation-induced electric potential,

where thermomechanical responses are harvested for successive actuation of ferroelectric films. We have also demonstrated localized photothermic vaporization under ambient outdoor conditions using simple prototypes. This work suggests that the cost-effective CS may be used to supplement the existing solar desalination technology by triggering localized steam generation well below the boiling point. In the context where water supply infrastructures are poor and settings are off-grid/remote, photothermic distillation/desalination and energy generation is an economical alternative owing to its potentially low maintenance requirements, low capital investment, and portability.

Supporting Information

Supporting Information is available from the Wiley Online Library or from the author.

Acknowledgements

This research is supported by the Singapore Ministry of National Development and the National Research Foundation, Prime Minister's Office under the Land and Liveability National Innovation Challenge (L2 NIC) Research Programme (L2 NIC Award No. L2NICFP2-2015-3). The authors thank Park Systems (Singapore) for the help in the AFM and SThM imaging.

Conflict of Interest

The authors declare no conflict of interest.

Keywords

carbon sponges, electricity generation, interfacial heating, photothermic vaporization, solar water evaporation

Received: August 6, 2017

Revised: November 27, 2017

Published online: January 29, 2018

- [1] G. Ni, G. Li, S. V. Borisikina, H. Li, W. Yang, T. Zhang, G. Chen, *Nat. Energy* **2016**, *1*, 16126.
- [2] G. Xue, Y. Xu, T. Ding, J. Li, J. Yin, W. Fei, Y. Cao, J. Yu, L. Yuan, L. Gong, J. Chen, S. Deng, J. Zhou, W. Guo, *Nat. Nanotechnol.* **2017**, *12*, 317.
- [3] L. Zhou, Y. Tan, J. Wang, W. Xu, Y. Yuan, W. Cai, S. Zhu, J. Zhu, *Nat. Photonics* **2016**, *10*, 393.
- [4] N. S. Lewis, *Science* **2016**, *351*, aad1920.
- [5] J. Yin, X. Li, J. Yu, Z. Zhang, J. Zhou, W. Guo, *Nat. Nanotechnol.* **2014**, *9*, 378.
- [6] J. Yin, Z. Zhang, X. Li, J. Yu, J. Zhou, Y. Chen, W. Guo, *Nat. Commun.* **2014**, *5*, 3582.
- [7] A. Polman, *ACS Nano* **2013**, *7*, 15.
- [8] X. Hu, W. Xu, L. Zhou, Y. Tan, Y. Wang, S. Zhu, J. Zhu, *Adv. Mater.* **2017**, *29*, 1604031.
- [9] Q. Jiang, L. Tian, K. K. Liu, S. Tadepalli, R. Raliya, P. Biswas, R. R. Naik, S. Singamaneni, *Adv. Mater.* **2016**, *28*, 9400.
- [10] Y. Liu, S. Yu, R. Feng, A. Bernard, Y. Liu, Y. Zhang, H. Duan, W. Shang, P. Tao, C. Song, *Adv. Mater.* **2015**, *27*, 2768.
- [11] M. Gao, P. K. N. Connor, G. W. Ho, *Energy Environ. Sci.* **2016**, *9*, 3151.
- [12] M. S. Zielinski, J.-W. Choi, T. La Grange, M. Modestino, S. M. H. Hashemi, Y. Pu, S. Birkhold, J. A. Hubbell, D. Psaltis, *Nano Lett.* **2016**, *16*, 2159.
- [13] L. Zhou, Y. Tan, D. Ji, B. Zhu, P. Zhang, J. Xu, Q. Gan, Z. Yu, J. Zhu, *Sci. Adv.* **2016**, *2*, e1501227.
- [14] L. Zhou, S. Zhuang, C. He, Y. Tan, Z. Wang, J. Zhu, *Nano Energy* **2017**, *32*, 195.
- [15] Y. Ito, Y. Tanabe, J. Han, T. Fujita, K. Tanigaki, M. Chen, *Adv. Mater.* **2015**, *27*, 4302.
- [16] J. Wang, Y. Li, L. Deng, N. Wei, Y. Weng, S. Dong, D. Qi, J. Qiu, X. Chen, T. Wu, *Adv. Mater.* **2017**, *29*, 1603730.
- [17] Z. Liu, H. Song, D. Ji, C. Li, A. Cheney, Y. Liu, N. Zhang, X. Zeng, B. Chen, J. Gao, Y. Li, X. Liu, D. Aga, S. Jiang, Z. Yu, Q. Gan, *Global Challenges* **2017**, *1*, 1600003.
- [18] X. Li, W. Xu, M. Tang, L. Zhou, B. Zhu, S. Zhu, J. Zhu, *Proc. Natl. Acad. Sci. USA* **2016**, *113*, 13953.
- [19] Y. Wang, L. Zhang, P. Wang, *ACS Sustainable Chem. Eng.* **2016**, *4*, 1223.
- [20] N. Xu, X. Hu, W. Xu, X. Li, L. Zhou, S. Zhu, J. Zhu, *Adv. Mater.* **2017**, *29*, 1606762.
- [21] J. Zhou, Z. Sun, M. Chen, J. Wang, W. Qiao, D. Long, L. Ling, *Adv. Funct. Mater.* **2016**, *26*, 5368.
- [22] M. Yang, M. Zhang, M. Kunioka, R. Yuge, T. Ichihashi, S. Iijima, M. Yudasaka, *Carbon* **2015**, *83*, 15.
- [23] G. Modugno, F. Ksar, A. Battigelli, J. Russier, P. Lonchambon, E. Eleto da Silva, C. Ménard-Moyon, B. Soula, A.-M. Galibert, M. Pinault, E. Flahaut, M. Mayne-L'Hermite, A. Bianco, *Carbon* **2016**, *100*, 367.
- [24] L. Zhu, Y. Yin, C.-F. Wang, S. Chen, *J. Mater. Chem. C* **2013**, *1*, 4925.
- [25] Q. Liu, B. Guo, Z. Rao, B. Zhang, J. R. Gong, *Nano Lett.* **2013**, *13*, 2436.
- [26] L. Wang, Y. Wang, T. Xu, H. Liao, C. Yao, Y. Liu, Z. Li, Z. Chen, D. Pan, L. Sun, M. Wu, *Nat. Commun.* **2014**, *5*, 5357.
- [27] G. Wang, Y. Fu, X. Ma, W. Pi, D. Liu, X. Wang, *Carbon* **2017**, *114*, 117.
- [28] H. Ghasemi, G. Ni, A. M. Marconnet, J. Loomis, S. Yerci, N. Miljkovic, G. Chen, *Nat. Commun.* **2014**, *5*, 4449.
- [29] S. Chen, G. He, H. Hu, S. Jin, Y. Zhou, Y. He, S. He, F. Zhao, H. Hou, *Energy Environ. Sci.* **2013**, *6*, 2435.
- [30] D. Hulicova-Jurcakova, M. Seredych, G. Q. Lu, T. J. Bandosz, *Adv. Funct. Mater.* **2009**, *19*, 438.
- [31] X. Wu, X. Yu, Z. Lin, J. Huang, L. Cao, B. Zhang, Y. Zhan, H. Meng, Y. Zhu, Y. Zhang, *Int. J. Hydrogen Energy* **2016**, *41*, 14111.
- [32] Y. Zhou, L. Zhang, W. Huang, Q. Kong, X. Fan, M. Wang, J. Shi, *Carbon* **2016**, *99*, 111.
- [33] Y. Ganesan, C. Peng, Y. Lu, L. Ci, A. Srivastava, P. M. Ajayan, J. Lou, *ACS Nano* **2010**, *4*, 7637.
- [34] A. Soudi, R. D. Dawson, Y. Gu, *ACS Nano* **2011**, *5*, 255.
- [35] S. Huxtable, D. G. Cahill, V. Fauconnier, J. O. White, J.-C. Zhao, *Nat. Mater.* **2004**, *3*, 298.
- [36] A. A. Wilson, M. Munoz Rojo, B. Abad, J. A. Perez, J. Maiz, J. Schomacker, M. Martin-Gonzalez, D.-A. Borca-Tasciuc, T. Borca-Tasciuc, *Nanoscale* **2015**, *7*, 15404.
- [37] G. Fugallo, A. Cepellotti, L. Paulatto, M. Lazzeri, N. Marzari, F. Mauri, *Nano Lett.* **2014**, *14*, 6109.
- [38] S. M. Sajadi, N. Farokhnia, P. Irajizad, M. Hasnain, H. Ghasemi, *J. Mater. Chem. A* **2016**, *4*, 4700.
- [39] F. Gao, W. Li, X. Wang, X. Fang, M. Ma, *Nano Energy* **2016**, *22*, 19.
- [40] X.-Q. Wang, C. F. Tan, K. H. Chan, K. Xu, M. Hong, S.-W. Kim, G. W. Ho, *ACS Nano* **2017**, *11*, 10568.
- [41] Q. Leng, L. Chen, H. Guo, J. Liu, G. Liu, C. Hu, Y. Xi, *J. Mater. Chem. A* **2014**, *2*, 11940.
- [42] H. Jin, G. Lin, L. Bai, A. Zeiny, D. Wen, *Nano Energy* **2016**, *28*, 397.